Journal of Manufacturing Processes 173 (2026) 817–832

Contents lists available at ScienceDirect

Journal of Manufacturing Processes

journal homepage: www.elsevier.com/locate/manpro

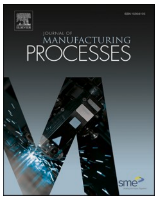

Microstructure control to enhance low temperature and cryogenic wear behavior of Inconel 718 produced by laser powder bed fusion

Yılmaz Küçük [a], Ozkan Gokcekaya [b,*], Ali Günen [c,*], Mustafa Sabri Gök [a], Abdollah Bahador [d], Takayoshi Nakano [b], Gürel Çam [e,f]

[a] *Bartın University, Faculty of Engineering, Architecture and Design, Department of Mechanical Engineering, Bartın, Turkey*
[b] *Graduate School of Engineering, Division of Materials and Manufacturing Science, The University of Osaka, 565-0871 Suita, Osaka, Japan*
[c] *Iskenderun Technical University, Faculty of Engineering and Natural Sciences, Department of Metallurgy and Materials Engineering, 31200 Iskenderun-Hatay, Turkey*
[d] *Materials Processing Institute, Eston Rd, Middlesbrough, TS6 6US, United Kingdom*
[e] *Iskenderun Technical University, Faculty of Engineering and Natural Sciences, Department of Mechanical Engineering, 31200 Iskenderun-Hatay, Turkey*
[f] *Istanbul Gedik University, Department of Metallurgy and Materials Engineering, Istanbul, Turkey*

ARTICLE INFO

Keywords:
Laser powder bed fusion
Laser energy density
Microstructure
Wear
Friction

ABSTRACT

In this study, the wear behavior of Inconel 718 samples produced using the Laser Powder Bed Fusion (LPBF) technique at varying laser energy densities was investigated under room temperature, subzero, and cryogenic conditions. Wear tests were conducted using a ball-on-flat configuration with a forward-backward linear motion. The tests were performed under dry sliding conditions against a 6 mm diameter WC-Co abrasive ball, applying a 10 N load, a sliding speed of 20 mm/s, and a test duration of 10 min at temperatures of 23 °C, −40 °C, and −150 °C. The findings of the study revealed that increasing laser energy density led to higher nanohardness (H) values, while the elastic modulus (E) decreased inversely. The wear rates were found to correlate with the H/E and H^3/E^2 ratios. Evaluation of the effect of ambient temperature on wear behavior exhibited that wear volume loss was highest at −40 °C, while plastic deformation and abrasive wear mechanisms were predominant at room temperature. While wear debris spread and exfoliation type wear were observed at −40 °C, the lowest volume losses occurred under cryogenic conditions despite obtaining smoother wear surfaces. COF values were similar at RT and − 40 °C, but decreased significantly at cryogenic temperature. Oxide formation was observed at RT while no oxide formation was detected at subzero and cryogenic temperatures.

1. Introduction

The demand for high-performance materials capable of withstanding extreme conditions has risen significantly with advancements in aerospace, energy, and cryogenic engineering. Cryogenic applications, such as liquid fuel storage, liquefied natural gas (LNG) transport, and superconducting technologies, demand materials with exceptional mechanical properties, corrosion resistance, and thermal stability at temperatures approaching absolute zero [1,2]. Traditional materials often fail under these extreme conditions due to brittle fracture, thermal contraction, or microstructural instabilities [3]. In this context, nickel-based superalloys like Inconel 718 (IN718) have emerged as a promising material, offering a compelling solution due to their robust performance and proven reliability [4–8].

IN718, a precipitation-hardened nickel-chromium alloy, is distinguished by its exceptional combination of mechanical strength, fatigue resistance, and corrosion tolerance across a wide temperature spectrum [6]. Its superior performance stems from a combination of γ' (Ni_3Nb) and γ″ ($Ni_3(Al,Ti)$) precipitate phases, which reinforce its microstructure. Moreover, Inconel 718's low coefficient of thermal expansion and high fracture toughness ensure its stability under extreme thermal cycling, a critical requirement in cryogenic engineering [9]. However, as applications demand even higher precision and enhanced performance, traditional manufacturing methods encounter limitations in tailoring the microstructure and mechanical properties required for specific use cases. This has paved the way for additive manufacturing (AM) techniques, which are revolutionizing the production of IN718 components with unprecedented design flexibility and microstructural control [10].

Additive manufacturing (AM), particularly laser powder bed fusion

---

* Corresponding authors.
E-mail addresses: ozkan@mat.eng.osaka-u.ac.jp (O. Gokcekaya), ali.gunen@iste.edu.tr (A. Günen).

https://doi.org/10.1016/j.jmapro.2026.07.009
Received 8 July 2025; Received in revised form 11 March 2026; Accepted 2 July 2026

(LPBF), has redefined the boundaries of manufacturing by enabling the production of complex geometries and bespoke components while minimizing material waste [11–13]. For IN718, AM not only addresses challenges associated with conventional fabrication, such as machining difficulties and weldability issues, but also opens new frontiers in microstructural optimization. A crucial advantage of AM lies in its ability to control crystallographic texture and grain structure [10], which directly influences mechanical and thermal properties under cryogenic conditions [6].

During LPBF processes, localized melting and rapid solidification result in unique microstructural characteristics. In the LPBF method, extremely rapid rates of melting and solidification are involved because of the local interaction between the laser beam and the powder bed. The rates of cooling in the LPBF method are in the order of 10^6–10^7 K/s. These are several orders higher than the rates found in the conventional casting method. Rapid rates of solidification in the LPBF method are known to produce microstructures such as cells and dendrites, microsegregation of alloying elements, and metastable phase compositions, which are known to significantly affect the mechanical and tribological properties of additively manufactured Inconel 718. For instance, crystallographic textures such as $\langle 001 \rangle$ or $\langle 101 \rangle$ orientations can be tailored by controlling process parameters like laser power, scan speed, and build orientation [14]. A $\langle 001 \rangle$ texture, for example, is associated with enhanced tensile strength along the build direction, whereas a $< 101>$ orientation may improve creep resistance. By optimizing these textures [10], AM enables the development of IN718 components with anisotropic properties specifically tailored for the demands of cryogenic environments. Additionally, the flexibility of AM allows for the production of polycrystalline structures with refined grain sizes, further enhancing fracture toughness and reducing the likelihood of microcrack propagation at low temperatures [15].

Beyond texture control, AM facilitates the inclusion of gradient microstructures and functionally graded materials (FGMs), enabling seamless integration of components with varying properties [11]. This capability is particularly valuable in cryogenic applications where thermal gradients and mechanical stresses are pronounced. Moreover, AM's layer-by-layer approach permits the incorporation of lattice structures and internal channels, improving thermal management and reducing weight, critical for applications like aerospace cryogenics [16].

The tribological behavior of additively manufactured Inconel 718 has been investigated in several studies. For example, Samuel et al. (2020) investigated the high-temperature dry sliding wear behavior of LPBF-fabricated Inconel 718 and found that the coefficient of friction and the weight loss were reduced at higher temperatures because of the protective oxide layers formed on the surface during the dry sliding wear process [17]. Recently, the effects of heat treatment on the tribological behavior of LPBF-fabricated Inconel 718 have been studied by Naskar et al. (2024). The authors found that the precipitation behavior of strengthening phases has significant effects on friction behavior and wear resistance [18]. The above studies clearly show that the process parameters and the microstructural characteristics developed during LPBF have significant effects on the tribological behavior of Inconel 718.

Despite its substantial potential, AM of Inconel 718 alloy for cryogenic applications still faces some important issues to be addressed [19]. These issues, such as residual stress, internal porosity, and microstructural anisotropy, need to be effectively addressed to ensure the reliability of the components under harsh service conditions. To address the aforementioned issues associated with AM of IN718 alloy, advanced post-processing methods, such as hot isostatic pressing, are used to optimize the microstructure of the alloy, thereby enhancing its mechanical properties [20,21]. In addition, the ability to simulate the microstructural evolution of materials, such as IN718 alloy, under cryogenic conditions, as offered by modeling, is crucial to promote the wider application of AM-fabricated IN718 alloy components.

Clearly, the excellent combination of mechanical properties, as well as corrosion resistance, of Inconel 718 alloy, along with the versatility of AM technology, provides substantial opportunities to explore new applications of this alloy, particularly under harsh service conditions. In this regard, the ability to optimize the microstructure of AM-fabricated IN718 alloy, such as grain morphology, crystal texture, etc., provides substantial opportunities to improve the reliability of IN718 alloy components under cryogenic conditions. It is expected that with the advancement of the research in this area, these developments will continue to increase the potential of the application of additively manufactured materials in cryogenic technologies.

Although there have been studies on the microstructural characteristics of LPBF-produced Inconel 718, the relationship between these unique microstructural characteristics and the tribological properties under different environmental conditions has not been fully clarified. In addition, the influence of these microstructural characteristics on the wear properties at ambient and cryogenic temperatures has not been explored. Therefore, the aim of the present study is to examine the microstructural characteristics and wear properties of LPBF-produced Inconel 718 at ambient and cryogenic temperatures.

2. Material and method

2.1. Fabrication of IN718 by LPBF

IN718 samples were fabricated by LPBF (EOS M290), using commercial gas-atomized IN718 powder (EOS Metal Solutions) with 20–55 μm particle size distribution and standard composition as illustrated in Fig. 1(a). The LPBF fabrications were carried out at 80 °C base temperature to compensate for the heat accumulation during the process which may cause disturbance to fabrication otherwise. The LPBF process was performed in a high-purity argon gas atmosphere to avoid oxidation during the fabrication. A bidirectional scan strategy (X scan) was applied to fabricate 10 × 30 × 30 mm samples as schematically given in Fig. 1(b) to promote strong and stable texture formation. Previously established process parameters which formed unique microstructural features [4] were the subjects of this study according to the investigation on processability window. The details of the IN718 process conditions which are of interest to this study are mentioned in Section 3.1. with the data presented in Fig. 2. Three distinctive microstructures, presented as lamella, single-crystal-like, and poly-crystal microstructures [10] are investigated for their cryogenic wear performance. The lamella texture (LPBF-1) was formed with laser power of 360 W and 1000 mm/s scan speed processing parameters while increase in scan speed to 1400 mm/s resulted in single-crystal like texture (LPBF-2). With the scan speed of 1400 mm/s and decrease in laser power to 180 W caused disappearance of texture and resulted in poly-crystal microstructure (LPBF-3). Besides these process parameters, powder layer thickness (h = 0.040 mm) and hatch space (d = 0.080 mm) were kept constant as listed in Table 1. Therefore, the laser energy density (E) of the LPBF-fabricated IN718 samples can be calculated by $E = \frac{P}{V \times h \times d}$ and the unique microstructure formation of lamella, single-crystal like, and poly-crystal were in the descending order as $E_{\text{LPBF-1}} > E_{\text{LPBF-2}} > E_{\text{LPBF-3}}$.

2.2. Wear tests

Inconel 718 alloy is known to exhibit increased hardness at low ambient temperatures, particularly increased ductility at cryogenic temperatures. To determine the possible differences in sample microstructure and mechanical properties due to additive manufacturing process parameters, and to assess the wear behavior of Inconel 718 at different ambient temperatures, wear test parameters were selected as shown in Table 2. After the surfaces of the LPBF-1, LPBF-2 and LPBF-3 samples produced in dimensions of 10x30x30 mm were cleaned with alcohol, they were connected to the test device in a direction perpendicular to the laser scan direction (YZ plane) in order to determine the effect of the existing surface texture on the wear behavior (Fig. 1(c)). As

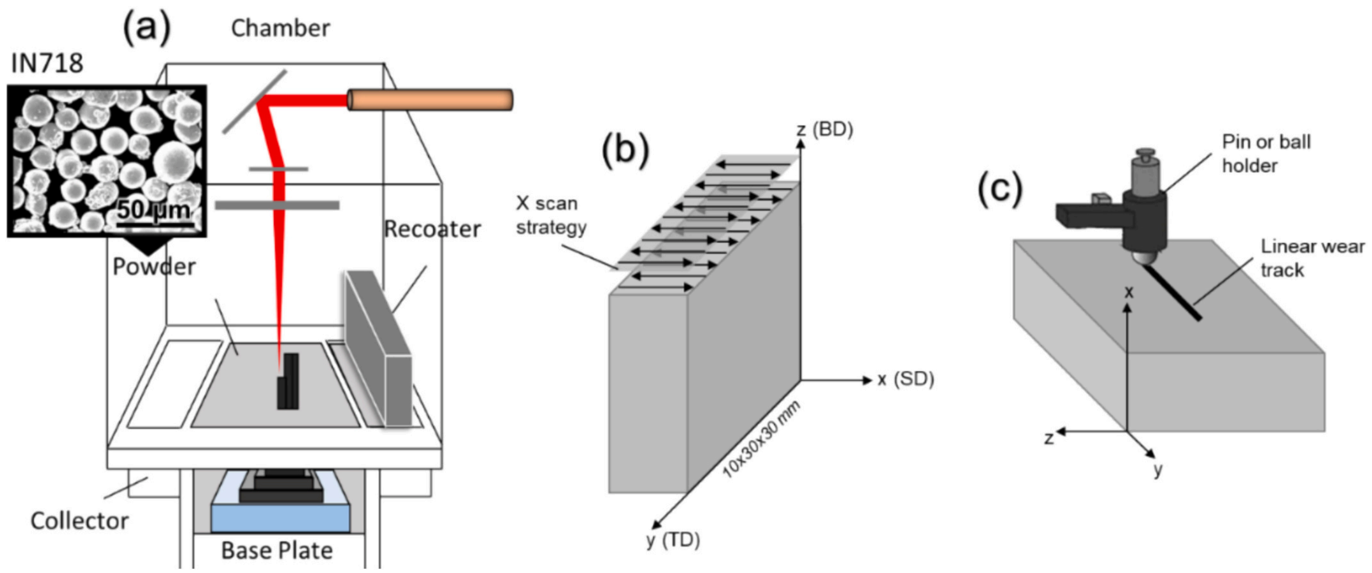

Fig. 1. Schematic illustration of (a) IN718 powder processed by LPBF and (b) the final 10 × 10 × 30 mm samples to conduct (c) cryogenic wear tests.

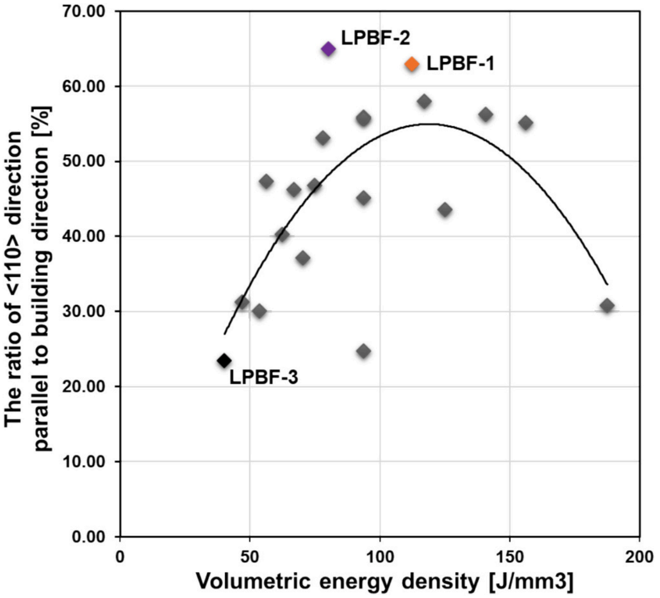

Fig. 2. The change in the ratio of <101> direction of the crystallographic orientation along the building direction with respect to the energy density.

Table 1
LPBF process parameters to control the microstructural features of IN718.

Samples	Laser power, *P* (W)	Scan speed, *V* (mm/s)	Hatch space, *d* (mm)	Powder layer thickness, *h* (mm)	Laser energy density, *E* (J/mm^3)
LPBF-1	360	1000	0.08	0.04	112.5
LPBF-2	360	1400	0.08	0.04	80.4
LPBF-3	180	1400	0.08	0.04	40.2

Table 2
Wear test parameters.

Abrasive material	Load (N)	Sliding speed (mm/s)	Test duration (min)	Ambient temperature (°C)
6 mm WC ball (Hardness: 19 GPa)	10	20	10	23, −40, −150

for the working principle of the cooling system, the compressed air taken from the air compressor was passed through the air filter and the dryer filter and then cooled to −30 °C with a pre-cooling process. After this process, the pre-cooled compressed air was passed through the radiator type cooling pipes in the liquid nitrogen tank and its temperature was reduced to −150 °C. The PLC controlled cooling system adjusts the ambient temperature instantly and precisely (±5 °C) with a temperature measuring probe placed inside the tribotest chamber. Compressed air is supplied to the system until the ambient temperature of the tribotester chamber reaches the desired value (cooling rate − 10 °C/min). Then, it is cut off by a pneumatic valve. Before starting the test, each sample is kept in the cooled chamber for 30 min to reach stabilization with the set ambient temperature. Before starting the test, each sample is kept in the cooled chamber for 30 min to reach equilibrium with the set ambient temperature. All tests were designed as dry sliding wear tests and were carried out in the ball-on-flat system (Tribotester: Turkyus™, Turkey) and in forward-backward linear motion mode. All tests were repeated 3 times to check the consistency of the results. Additionally, COF graphs were derived from the tangential load values recorded simultaneously during each wear test.

2.3. Characterization

The sample surfaces were initially ground using 320–2500 grit sandpapers for microstructural observation. Subsequently, the specimens were polished with a polishing cloth using a 0.01 µm alumina solution. Field Emission Scanning Electron Microscope (FESEM) was utilized in order to capture the SEM images and EDS spectrum related to the investigation (JIB-4610F, JEOL). Further detailed microstructure analyses were conducted using a FESEM equipment equipped with EBSD detector (Aztec HKL, Oxford Instruments) and the obtained data were analyzed using analysis software (HKL Channel5, Oxford Instruments, UK) to obtain inverse pole figure (IPF) maps, corresponding pole figures, grain size distribution, grain boundary misorientation, qualitative and quantitative analyses of high-angle grain boundaries (HAGBs), Kernel average misorientation (KAM) distribution, and geometrically necessary dislocation (GND).The phase analysis of the IN718 samples was carried out by X-ray diffraction (XRD, RINT-2500 V, Rigaku, Japan) using Cu Kα radiation with a wavelength of 0.154 nm. The XRD data were obtained through point scanning in the 2θ angular range from 40° to 100° with a step size of 0.02° and a scan time of 2 s per step at room temperature. Further confirmation of phase analyses was carried out by transmission electron microscope (TEM, JEOL JEM-3010) operated at 300 kV.

For the assessment of mechanical properties regarding the microstructural features at room temperature, nanoindentation (ENT-1100a, ELONIX, Japan) tests were carried out using a Berkovich tip at a force of 10 mN. The nanoindentation tests were performed according to Oliver–Pharr method, and a Poisson's ratio of 0.30, which is generally used for metallic materials [22], was taken into consideration while calculating the hardness and elastic modulus values. Further, the calculated values for hardness and elastic modulus were found by taking the average values in the stable range of indentation depth, and the corresponding standard deviations were calculated from multiple indents performed in the tests.

The wear track profiles obtained from the wear tests were analyzed using a 3D optical profilometer (Filmetrics Profilm 3D, USA). The wear volume loss values were calculated by multiplying the cross-sectional area of the wear track by the track length. Scanning electron microscopy (SEM) was employed to examine the worn surfaces in order to evaluate the wear mechanisms and surface microstructure. Furthermore, oxide formation on the wear surface was identified through energy-dispersive X-ray spectroscopy (EDS) line analysis.

3. Results and discussion

3.1. Microstructural features

Controlling crystallographic orientation is crucial for tailoring mechanical properties in IN718 because the arrangement of crystal lattices significantly impacts its mechanical behavior. By manipulating crystal orientation, it is possible to achieve desired strengths, hardness, ductility, and other mechanical characteristics in anisotropic materials [8]. The variation of the crystal orientation formed in this study was unique compared to the previous studies with <001> cubic or fiber textures [23–26], where the process conditions in this study produced a {101} texture parallel to the build direction as discussed in the following sections. Moreover, it is important to note that the trend of ⟨101⟩ orientation ratio exhibited an increase and then a decrease regarding the increase in energy density (Fig. 2).

To quantitatively characterize the evolved texture, the degree of orientations (p) of {011} with respect to the build direction were calculated based on the Euler angles obtained by EBSD as follows: $p_{\{hkl\}} = \langle cos^2\alpha_{\{hkl\}} \rangle$, where $\alpha_{\{hkl\}}$ shows the angle of {011} from the build direction derived from Euler angles at each analysis point in EBSD, and the angle brackets represent the average at all analyzed points as presented in Fig. 2 for all the samples in process window. Besides, the samples of interest in this study were marked on Fig. 2, indicating strong texture formation in LPBF-1 and LPBF-2 while LPBF-3 was chosen as a nontextured for comparison purpose.

The specimens produced by the Laser Powder Bed Fusion (LPBF) process exhibit a distinguishable microstructure characterized by melt pool boundaries and laser scan tracks. The variation in microstructural features observed under different laser energy densities in the LPBF process is primarily attributed to changes in the size and shape of the melt pool [10,27–29]. The melt pool shape and size of In718 samples of interest in this study were observed and the representing microscopic images were given in Fig. 3. Additionally, the compositional differences regarding melt pool boundary and melt pool center regions were reported with the attached Table in Fig. 3 comparatively to the commercial powder composition.

Different phases in the microstructure can affect the mechanical properties of the parts produced using LPBF. NbC, Ni_3Nb (δ phase) and also Laves phases and some other intermetallic compounds are present in the IN718 matrix structure. Ni_3Nb (δ phase), which is orthorhombic, can affect the grain size and grain boundary motion. γ″- $Ni_3(Nb/Al/Ti)$ phase with a cubic crystal structure and γ'- $Ni_3(Al/Ti)$ phase with a body-centered tetragonal structure can provide strength to the matrix [30].

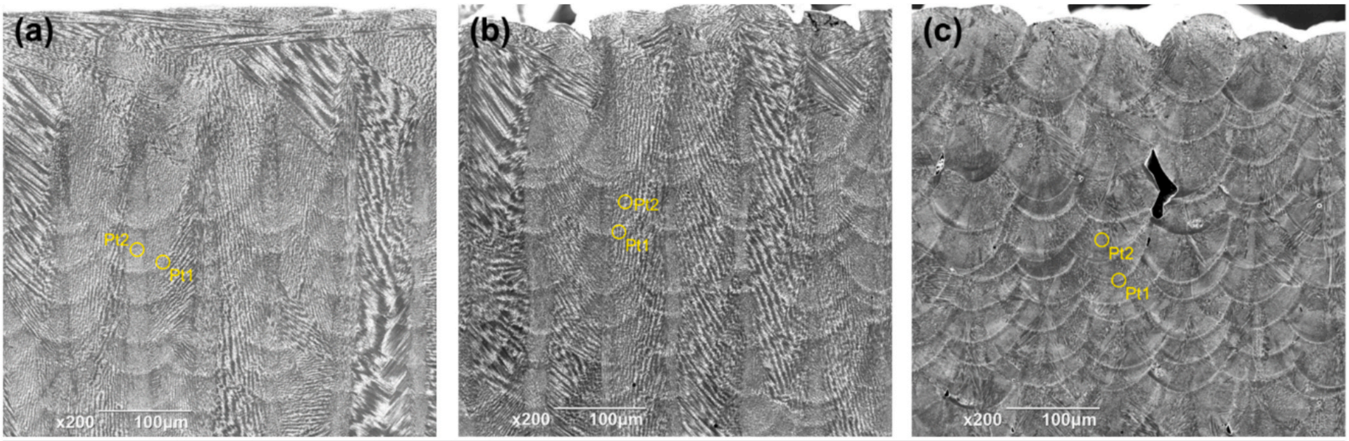

Sample	EDS (Wt. %)	Al	Ti	Cr	Fe	Co	Ni	Nb	Mo
IN718	*Min*	*0.2*	*0.65*	*17*	*Bal*	-	*50*	*4.75*	*2.8*
powder	*Max*	*0.8*	*1.15*	*21*	*Bal*	*1.0*	*55*	*5.5*	*3.3*
LPBF-1	Pt1	0.57	1.04	19.25	19.02	0.02	51.52	4.90	3.66
	Pt2	0.73	1.10	18.91	18.30	0.23	51.07	5.70	3.95
LPBF-2	Pt1	0.57	1.12	18.35	17.71	0.05	51.37	6.85	3.97
	Pt2	0.60	1.19	19.15	18.62	0.06	51.06	5.50	3.83
LPBF-3	Pt1	0.65	1.24	18.78	17.65	0.10	51.55	6.29	3.76
	Pt2	0.63	1.08	19.31	18.30	0.15	51.76	5.35	3.43

Pt1: Meltpool boundary
Pt2: Meltpool center

Fig. 3. Electron microscopy images of (a) LPBF-1, (b) LPBF-2, and (c) LPBF-3 showing the melt pool size with the compositional analyses on melt pool boundary (Pt1) and center (Pt2) regions.

However, Ni_3Nb (δ phase) and also Laves phases are generally observed as grain segregations in the microstructure. Laves phases are generally observed at the decomposition boundaries where there is higher Nb, C and Mo concentration [31–34]. These microsegregations can also be seen due to the rapid grain growth resulting from the higher cooling rate involved in the LPBF process. In particular, studies have been conducted on the reduction of Laves phases, which act as a site and pathway for crack propagation, facilitating the development of enhanced mechanical strength and influencing the dominant wear mechanisms [35,36]. However, according to XRD patterns, all LBPF samples exhibited only FCC Cr-Ni–Fe structure (ICDD Card No: 00–031-0619), no other phase formation or precipitation was observed. The high intensity peak in LBPF samples was detected as the (200) peak at 50.65 degrees. This can be attributed to the fact that due to epitaxial growth during layer-by-layer fabrication of the LPBF process, IN718 grains grow along (001) preferential growth directions and the LPBF process forms (001) dominant grains with unique microstructural features depending on the laser energy density [4,10].

Further detailed phase analyses were carried out to confirm the presence of precipitates, revealing no detectable precipitations, as expected and as reported previously [37]. The selected area electron diffraction (SAED) pattern (Fig. 4(b)) obtained from the [001] zone axis of the IN718 fcc matrix. The LPBF-1 sample, in which the cooling rate is supposed to be the smallest and the precipitation could be most likely to occur among the three conditions examined (LPBF-1/2/3). No diffraction spots other than the fcc γ phase were observed. The dark-field image taken using the encircled (invisible) spot from (001)γ'/(002)γ'', representing no visible precipitates. This is due to the ultra-rapid cooling rate ($\sim 10^7$ K/s) achieved during LPBF, preventing the formation of precipitate phases.

The microstructural features of LPBF-fabricated IN718 were given in Fig. 5 regarding crystallographic orientation with IPF maps and pole figures with the HAGB distribution, moreover, the texture formation was illustrated considering the melt pool shape as reported in Fig. 3. As the melt pool bottom curvature flattened, the minor <001> texture formation was evident for LPBF-1 condition at the center of the melt pool, thus, forming lamella texture with major <101> and minor <001> grain orientation as identified by pole figure. However, with decrease in laser energy density LPBF-2 condition formed less curved melt pool at the bottom region, thus, preventing a continuous <001> texture development. Therefore, the difference in pole figure as {001} orientation was not detected for LPBF-2 compared to LPBF-1. LPBF-3 condition with significantly low laser energy density, therefore containing lack of fusion and unmelted powders as shown in Fig. 3, had small melt pool size and unstable cellular growth, resulting in polycrystal microstructure. The weak texture formation, resulting in polycrystal as defined in this study, was evident from the pole figure comparison as the maximum intensity was set to 10.0, indicated with the scale bar. This laser energy dependent melt pool shape was the primary reason for the texture development with the differences in thermal characteristics, affecting cooling rate and stability of thermal gradient, therefore determining the cellular growth direction and stability. This aspect of microstructure formation has been discussed in our previous report in detail [10].

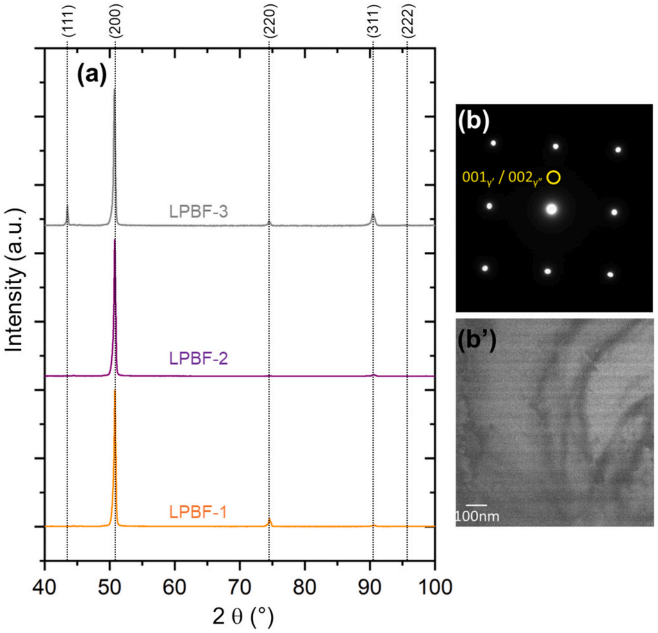

Fig. 4. (a) XRD patterns of IN718 fabricated by LPBF with (b) the diffraction pattern and (b') the dark-field image to identify the precipitate γ' phase of LPBF-1 sample.

However, the effect of these distinctive microstructural features on wear properties in ambient temperature and cryogenic environment has not been investigated to the best of our knowledge. The texture formation related to the epitaxial growth determined the grain size in the build samples. With high laser energy input, epitaxial growth was supported for LPBF-1 and LPBF-2 samples, resulting in higher grain size (16.3 μm and 17.1 μm, respectively, Fig. 6). It is noteworthy to mention that the grain distribution in Fig. 6 presented the high ratio of small grain size formation in LPBF-1 as a result of minor <001> grain growth in melt pool center, thus, expected to increase hardness according to Hall-Petch relationship while providing low Young's moduli grain orientation to lower the overall rigidity of the sample [38]. However, LPBF-3 condition with small laser energy density and limited epitaxial growth capacity exhibited smaller grain size (13.2 μm). Variation in grain size and the consequent HAGB density is crucial for understanding the mechanical response of the microstructure regarding the Hall-Petch relationship. To note that while LPBF-1 had smaller average grain size than LPBF-2 owing to the minor <001> grain growth in the melt pool center dividing the grains, LPBF-2 with larger grain size exhibited higher density of HAGBs. This indicated that grain growth stability of LPBF-2 was not well established with the provided laser energy input, thus forming complicated grain morphologies and dense HAGB zones as shown in Fig. 5(c). The obvious effect of unstable melt pool and grain growth on HAGB density was presented in Fig. 5(c) for LPBF-3.

As the grain orientation and the grain size are important indicators for the mechanical response of IN718 [6], considering the single phase microstructure, it is possible to relate the hardness and Young's modulus of these LPBF-fabricated IN718 conditions to the microstructural features as discussed above.

The yield strength of LPBF-fabricated IN718 can be evaluated by the following strength mechanisms in principle: the intrinsic strength (σ_0) of pure nickel, grain boundary strengthening (σ_{GB}), solid solution strengthening ($\Delta\sigma_{SS}$), dislocation strengthening ($\Delta\sigma_b$), and precipitation strengthening ($\Delta\sigma_p$). Considering these strengthening mechanisms, the solid solution and precipitation strengthening can be disregarded owing to the compositional similarity and nonexistence of detectable precipitation owing to the rapid cooling rate ($\sim 10^7$ K/s) of the LPBF process. Therefore, the effect of grain boundary strengthening was discussed regarding the results presented in Fig. 6.

Moreover, the intrinsic strength (σ_0) and dislocation strengthening ($\Delta\sigma_b$) should be considered to distinguish the effect of microstructural differences on the strength of LPBF-fabricated IN718. In this regard, the importance of Taylor factor and AM-intrinsic deformation-induced misorientation, identified with KAM in this study, values would be prominent. Thus, crystallographic texture was expected to have a significant impact on the anisotropy in yield strength, since the activity of slip systems and the Schmid/ Taylor factor were closely related to the grain orientation [10]. In order to establish a correlation between microstructure and its cryogenic wear performance, it is important to clarify the differences in microstructures in terms of misorientation/ dislocations and Taylor factor of as-built samples. As Fig. 7 presented the

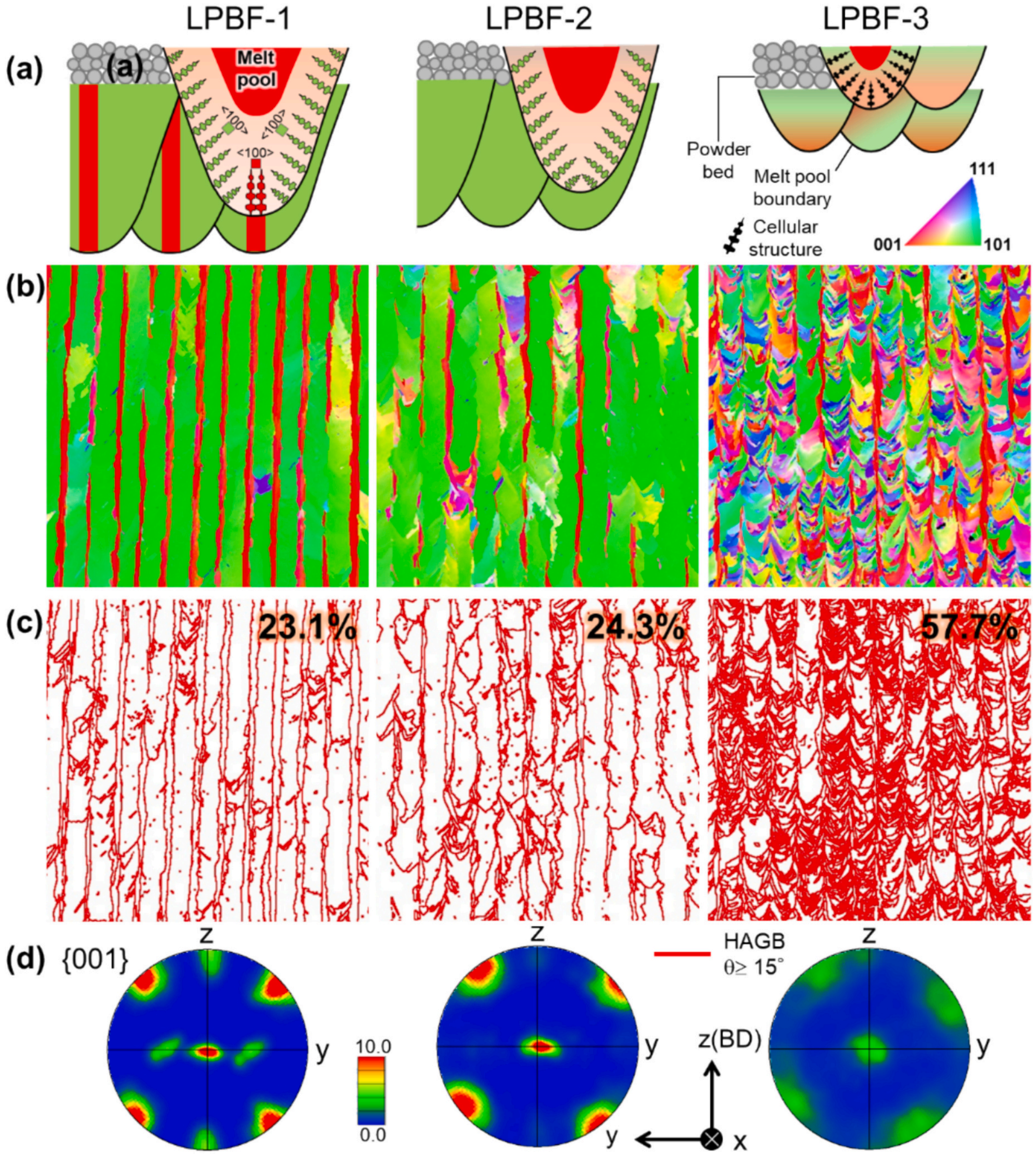

Fig. 5. (a) Schematic illustration of texture formation in melt pool of LPBF-fabricated IN718 during solidification and the actual experimental results confirming the illustrations: (b) Inverse pole figures (IPF), (c) high-angle grain boundary (HAGB) maps, and (d) corresponding {001} pole figures.

KAM and Taylor factor maps with the corresponding distributions, Taylor factor of LPBF-1/2/3 increased with the increase in laser energy density ($E_{\text{LPBF-1}} > E_{\text{LPBF-2}} > E_{\text{LPBF-3}}$–3.04, 3.29, 3.49 respectively). This indicated the requirement of higher stress to initiate slip system activation during deformation of LPBF-1 condition, as shown with the higher hardness value, which raised an expectation of improved performance under extreme wear conditions. Moreover, higher local misorientation in LPBF-1 compared to LPBF-2 was expected because of larger melt pools resulting in high volume solidification, which might correspond to cycling thermal stress during LPBF process. Besides, the high KAM was localized at the center of the melt pool, accumulated in minor <001> grains, where the solidification in a melt pool was finalized, thus, expected to be the high residual stress zones as reported in the recent literature [26]. Although LPBF-3 exhibited the highest KAM value with detectable large stress zones, the existence of lack of fusion defects was detrimental to its strengthening.

Overall, the microstructural features exhibited limited slip activation and high residual stress for LPBF-1 with no detectable defects, suggesting a good wear performance in extreme conditions [39]. Contrarily, LPBF-3 condition with lack of fusion defects would be expected to show the effect of inhomogeneity on the wear performance.

LPBF process parameters are basically laser power, scanning speed, consecutive scanning distance and powder layer thickness, which determine the laser energy density. These parameters significantly determine the microstructure of the parts produced using the LPBF method and the distribution of the phases it contains, and the mechanical properties such as porosity, hardness, and fracture toughness, which are close related to the microstructure [40–42]. Based on this, it

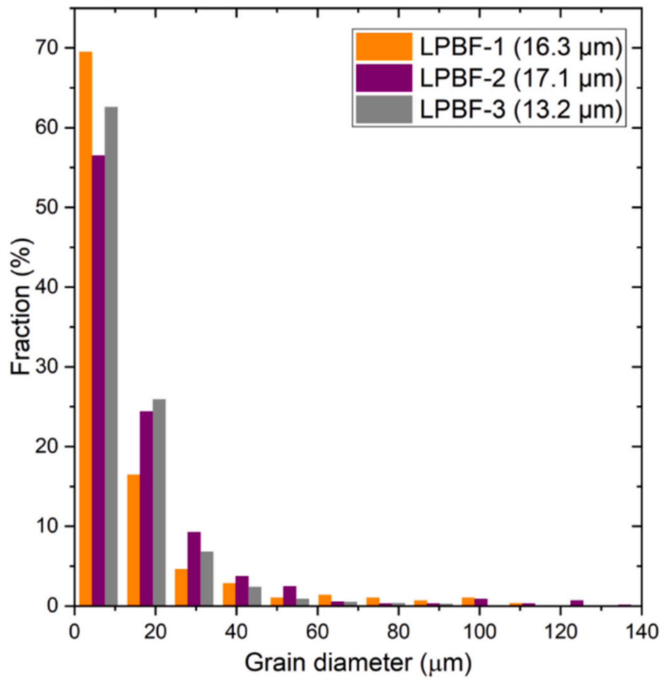

Fig. 6. Grain size distribution of LPBF-fabricated IN718.

can be concluded that the process parameters of LPBF directly influence the wear behavior of the material. In this study, the wear behavior of three samples - LPBF-1, LPBF-2, and LPBF-3 - produced with decreasing laser energy densities, was examined under varying ambient temperatures. Since wear resistance is directly related to the brittleness or fracture resistance of a material, it is quite appropriate to use nanoindentation data, which is a powerful technique in determining these values [43]. The average hardness and elastic modulus values obtained from nanoindentation tests of samples produced by the LPBF method, along with the calculated values of Hertzian contact pressure at each ambient temperature, are given in Table 3.

As shown in Table 3, at RT, the highest hardness was observed in the LPBF-1 sample, which was produced with the highest laser energy density. This was followed by the LPBF-2 and LPBF-3 samples, in descending order of laser energy density. In summary, an increase in laser energy density led to a corresponding increase in hardness. It is observed that the elastic modulus values vary inversely with laser energy density. This trend may be attributed to differences in lattice distortion caused by rapid cooling at higher laser scanning speeds [44]. Furthermore, when evaluating wear behavior, it is not sufficient to consider hardness alone; the hardness-to-elastic modulus ratio (H/E) must also be taken into account [45]. Specifically, the H/E ratio represents the material's resistance to cracking, while the H^3/E^2 ratio reflects its resistance to plastic deformation [46]. In other words, both H/E and H^3/E^2 are fundamental parameters for assessing a material's resistance to elastoplastic deformation, and they show positive correlations with fracture toughness and wear resistance [47,48]. It is known that Inconel 718 alloy increases in hardness, as well as in yield and tensile strength, at low ambient temperatures [49,50]. Furthermore, its lack of significant compromise to ductility and toughness makes it preferred engineering material even at low temperatures. Based on this, when the data in Table 3 is examined, it can be said that, due to the increasing hardness and modulus of elasticity values along with decreasing ambient temperature, the resistance to crack formation (H/E) and plastic deformation (H^3/E^2) will also be higher compared to RT. Based on the H/E ratios presented in Table 3, the LPBF-1 sample exhibits the highest fracture toughness at all ambient temperatures. This result can be attributed to a balanced cooling achieved through the combination of high laser power and relatively low scanning speed. The lower H/E ratios observed in the LPBF-2 and LPBF-3 samples indicate a proportional decrease in fracture toughness with decreasing laser energy density. Similarly, the H^3/E^2 values increase with laser energy density, with the highest value indicating the greatest resistance to elastoplastic deformation. Therefore, when both H/E and H^3/E^2 ratios are considered together, it is evident that the wear resistance decreases in the order of LPBF-1, LPBF-2, and LPBF-3, corresponding to the decreasing laser energy densities at all ambient temperatures.

However, with the decrease in laser energy density, it is highly probable that the number of pores and the ratio of particles remaining unmelted will inevitably increase. Pores and unmelted particles are the main defects that reduce the fracture toughness of parts produced with LPBF. It has been reported that the decrease in fracture toughness is due to the fact that fracture occurs along unmelted particles [51]. In addition, it can be stated that the particles remaining without melting not only reduce the surface bonding, but also that the thin oxide film formed on the surfaces of these particles may cause the fracture toughness to decrease [52]. In some studies, researchers also pointed out that since low and cryogenic ambient temperatures will further reduce the fracture toughness, differences will also occur in wear volume loss and wear mechanisms [53,54]. However, wear is a complex phenomenon in which both the mechanical properties of the contacting materials and the experimental conditions significantly influence the material's wear behavior. Therefore, the increase in yield strength, UTS, hardness, and modulus of elasticity of Inconel 718 alloy with decreasing ambient temperature [49] has a decisive effect on contact mechanics and directly affects elastoplastic contact pressure in wear [55,56]. In contact mechanics, defined by Hertz [57], in the case of contact between a rigid sphere and a flat surface, the radius of the contact circle "a", where the maximum contact pressure spreads over, is related to the indentation load P, the indenter radius R, and the elastic properties of the materials and is formulated as in Eq. (1).

$$a^3 = \frac{3PR}{4E^*} \tag{1}$$

where E^* is combined elastic modulus of contact bodies, which can be calculated using Eq. (2) [58].

$$\frac{1}{E^*} = \frac{(1-\nu_s{}^2)}{E_s} + \frac{(1-\nu_i{}^2)}{E_i} \tag{2}$$

where E_s and ν_s, and E_i and ν_i, describe the elastic modulus and Poisson's ratio of the specimen and the indenter, respectively.

According to Eq. (1), the contact radius (a), which determines the area where crack initiation and propagation first occur, decreases with increasing combined elastic modulus (E^*) value, and consequently, the maximum contact pressure generated also increases [59]. The maximum contact pressure (p_{max}) at the contact region can be formulated as in Eq. (3) [58].

$$p_{max} = \frac{1}{\pi}\left(\frac{6PE^*}{R^2}\right)^{1/3} \tag{3}$$

when Table 3 is examined, it is seen that the highest contact pressure values occur at an ambient temperature of −40 °C, followed by those at cryogenic temperatures, and the lowest values are obtained at RT. The main reason for this case is that the Poisson ratio and elastic modulus values of Inconel 718 alloy change at low ambient temperatures [50].

3.2. Wear rate evaluation

Wear is not an inherent property of the material, but rather a complex damage mechanism influenced by numerous independent factors, including microstructure, hardness, ambient temperature, and the specific experimental conditions employed. Fig. 8 presents the graphs of

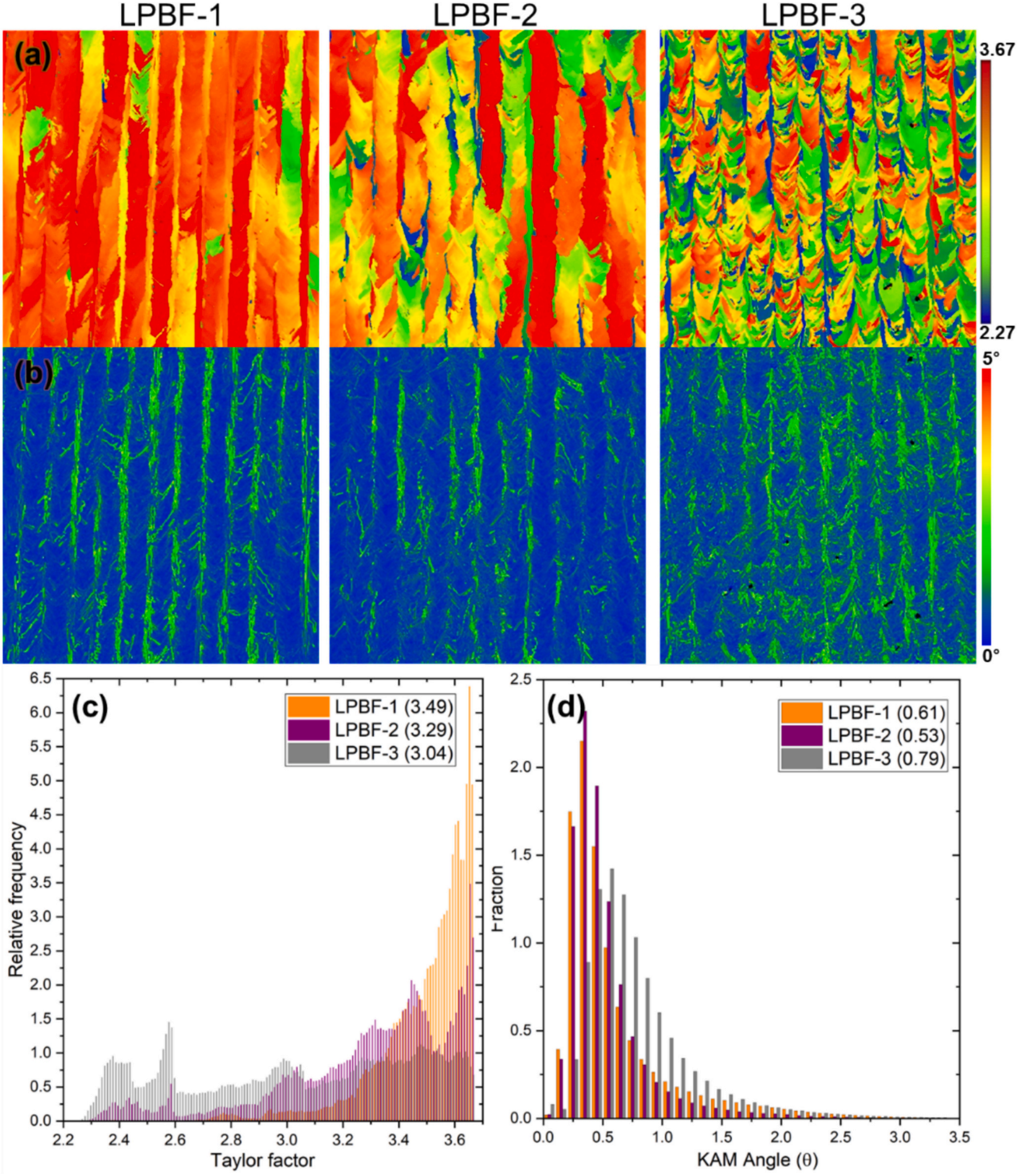

Fig. 7. (a) Taylor factor and (b) KAM mapping of LPBF-fabricated IN718 samples with corresponding (c) distribution of the Taylor factors and (d) KAM angle of each condition.

both instantaneous and average friction coefficient values recorded during the wear tests conducted at each ambient temperature.

Examination of Fig. 8 reveals that the coefficient of friction (COF) values for all LPBF samples at room temperature (RT) and − 40 °C are relatively similar, averaging between 0.54 and 0.59. However, the COF values at RT exhibit noticeable fluctuations throughout the experiment. This behavior may be attributed to the formation of interlayer boundaries resulting from the layer-by-layer nature of the LPBF manufacturing process. It is seen that at −40 °C, the COF value of the LPBF-1 sample with a lamellar structure was relatively low and stable at around 0.45 for the first 3 min from the beginning, but then it increased and followed a limited fluctuating course around 0.61. This behavior can be interpreted as an increase in tangential force resulting from the formation of brittle fracture and spallation zones within the contact

Table 3
Average values obtained from nanoindentation tests and calculated Hertzian contact pressure data for each test sample at different ambient temperatures.

Ambient temperature	Test sample code	Hardness	Elasticity modulus	Material's resistance to		Max. Hertzian contact pressure (MPa)
				Cracking	Plastic deformation	
		H (GPa)	E (GPa)	H/E	H^3/E^2	
RT	LPBF-1	6.51 ± 0.30	175.22 ± 8.84	0.0372	0.0090	1685
	LPBF-2	6.40 ± 0.27	182.02 ± 9.97	0.0352	0.0079	1719
	LPBF-3	6.36 ± 0.28	185.85 ± 10.15	0.0342	0.0074	1737
−40 °C	LPBF-1	6.91 ± 0.31	184.86 ± 9.98	0.0374	0.0097	1738
	LPBF-2	6.79 ± 0.28	192.03 ± 10.13	0.0354	0.0085	1772
	LPBF-3	6.75 ± 0.29	196.07 ± 10.62	0.0344	0.0080	1791
−150 °C	LPBF-1	7.55 ± 0.34	189.06 ± 10.14	0.0399	0.0120	1732
	LPBF-2	7.42 ± 0.31	196.40 ± 10.70	0.0378	0.0106	1766
	LPBF-3	7.37 ± 0.30	200.53 ± 10.98	0.0368	0.0100	1784

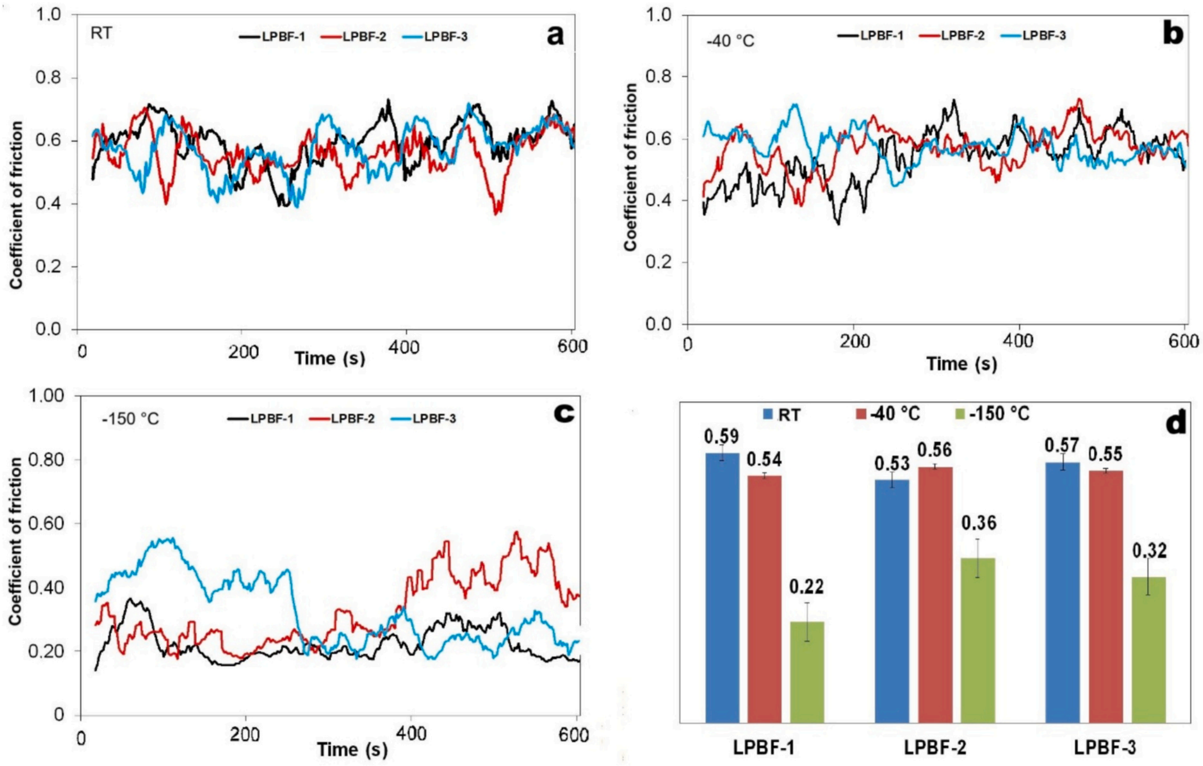

Fig. 8. CoF graphs and their average values recorded during the wear tests at different ambient temperatures a) RT b) -40 °C c) -150 °C d) average COF values.

area, beginning at the point where the COF starts to rise. In the LPBF-3 sample with a polycrystalline texture, the COF graph recorded at −40 °C exhibited only minor fluctuations throughout the experiment, without any significant variation. This behavior can be attributed to the sample's finer grain size relative to the other two samples and its production using the lowest laser energy density. As a result, the COF remained relatively stable, likely due to the influence of unmelted particles and spatter caused by incomplete fusion around them.

Examination of the instantaneous COF graphs recorded at −150 °C reveals that the lowest values for the LPBF-1, LPBF-2, and LPBF-3 samples are approximately 0.22, 0.36, and 0.32, respectively. As hardness increases, wear appears to be limited. Among the three, the LPBF-1 sample demonstrates a more stable COF trend throughout the test. In contrast, the LPBF-2 sample initially exhibits a COF value close to that of LPBF-1 - around 0.30 during the first five minutes - but subsequently increases and displays a fluctuating pattern, reaching approximately 0.50 toward the end of the experiment. This behavior is likely attributed to irregular fractures in the lower layers, particularly within the incomplete fusion zones at the laser scan boundaries, which become more pronounced as the wear scar depth increases over time. In contrast to LPBF-2, the LPBF-3 sample exhibits an opposite COF trend. Specifically, an average COF of approximately 0.40 was recorded during the first five minutes, after which it significantly decreased and stabilized in the range of 0.20–0.25 for the remainder of the test. This trend can be explained by the initial presence of irregular, rough surfaces resulting from early-stage wear, which gradually flattened over time. The resulting reduction in surface asperities likely led to a decrease in tangential shear stress, thereby lowering the COF. The specific wear rate values calculated as a result of the wear tests performed on samples produced with LPBF at different ambient temperatures are depicted in Fig. 9.

Examination of Fig. 9 reveals that the LPBF-1 sample, featuring a lamellar texture produced using the highest laser energy density, exhibits the lowest specific wear rate across all tested ambient temperatures. In contrast, the LPBF-2 and LPBF-3 samples - produced using medium and low laser energy densities, respectively - show progressively higher wear rates at all temperatures. These results are also quite consistent with the H/E and H^3/E^2 values presented in Table 3. In other

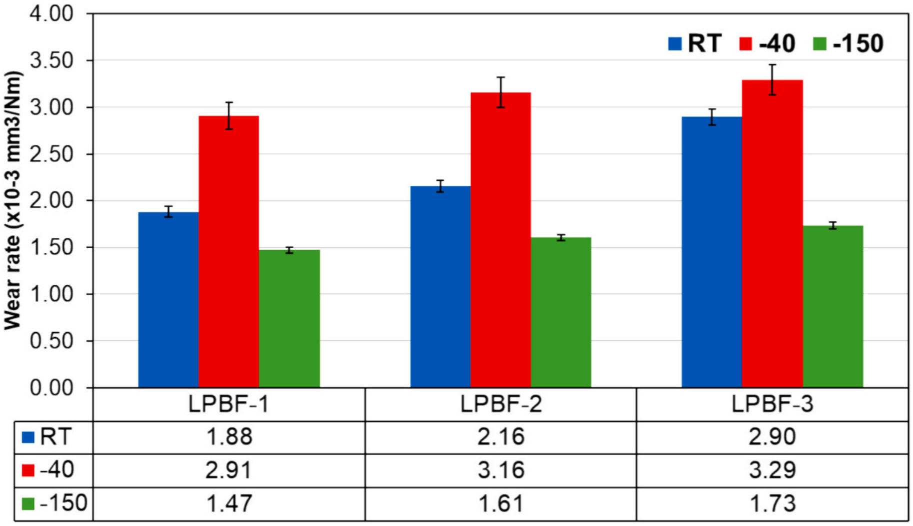

	LPBF-1	LPBF-2	LPBF-3
🟦 RT	1.88	2.16	2.90
🟥 -40	2.91	3.16	3.29
🟩 -150	1.47	1.61	1.73

Fig. 9. Average wear rate values of LPBF-fabricated IN718 samples after the wear tests at different ambient temperatures.

words, at all ambient temperatures, the lowest wear rate was obtained from the LPBF-1 sample, which has the highest hardness and is likely to contain the least porosity and microstructure defects due to the relatively lower cooling rate associated with the higher laser energy density used during its fabrication. In contrast, the LPBF-2 sample, produced with a 40% higher laser scanning speed than LPBF-1, experienced more rapid cooling, leading to grain refinement and an increased grain boundary length. These microstructural changes, combined with fusion defects and insufficient coalescence, are believed to have contributed to its higher wear rate. However, it has been reported that the distribution and nature of the existing insufficient fusion defects in the microstructure negatively impact fatigue life [60]. Thus, it is possible to say that fatigue-induced wear due to the effect of the opposite-direction repetitive movements applied in the reciprocating type wear test also contributes to the further increase in the total volume loss.

Regarding the effect of ambient temperature, previous studies have reported that the ductility -and consequently the fracture toughness - of parts produced by the LPBF process decreases at low temperatures [53]. However, according to the data obtained in this study, it is insufficient to explain the wear behavior solely by a decrease in ductility at lower ambient temperatures. Because an increase in ductility occurs at cryogenic temperatures, and the increase in H/E and H^3/E^2 values given in Table 3 proves this situation. Specifically, all LPBF samples exhibited the highest wear volume loss at an ambient temperature of −40 °C, compared to those tested at room temperature and cryogenic conditions. This explanation is further supported by the substantial amount of wear debris observed in the SEM images of the worn surfaces following the wear test at −40 °C (see Fig. 12). The determining factor in this increase in wear is the high contact pressure values. Although it has values indicating higher crack (H/E), and plastic deformation (H^3/E^2) resistance than RT, the higher contact pressure increased shear stresses, leading to crack formation and propagation in the contact area and creating conditions that increase spallation- and exfoliation-type wear. Furthermore, it can be argued that the solid lubricant effect of friction-induced oxide formation in RT, which prevents severe wear, mitigates the negative impact of the relatively low hardness and elastic modulus values in RT, thereby reducing crack resistance and plastic deformation resistance. As for cryogenic temperatures, it has been reported that cryogenic treatment not only enhances the microhardness of additively manufactured In718 samples but also improves their elongation [61]. To better understand this, it is helpful to recall the theoretical principles that govern hardness and the influence of temperature. Theoretically, a material's hardness is determined by atomic interactions, crystal lattice structure and type, and the number of valence electrons. Considering these factors, the theoretical hardness of materials can be expressed as follows [62]:

$$H_0 = const\ R_0/{a_0}^5 \tag{4}$$

where a_0 is the lattice parameter, R_0 is a parameter that can be adjusted for absolute temperature ($T = 0$ K), and *const* contains quantities such as the number of valence electrons, the coordination number, and some coefficients (all coefficients that appear when expressing the volume, the radius of the atoms, and the distance between atoms in terms of the lattice parameter).

The effect of temperature on hardness can be expressed as in Eq. (4) [59]:

$$H_T = H_0\left(\left(1+0,032(T/T_{max})^{5/4}\right)^{-5}(1-T/T_{max})\right)^{1/2} \tag{5}$$

where H_T represents the hardness value at any temperature T (K) and T_{max} represents the melting temperature (K) of the material.

The effect of crystal lattice contraction on the increase in material hardness at cryogenic temperatures should also be noted [63]. As the temperature decreases to cryogenic levels, the material undergoes volumetric shrinkage, leading to increased lattice stresses, which in turn contribute to the rise of hardness.

$$\alpha = V^{-1}\left(\partial V/_{\partial T}\right)P \tag{6}$$

where α is the expansion coefficient ($C^{-1} \times 10^{-6}$), V is the volume (mm^3) and P is the pressure (MPa). The volume changes from V_0 to VT as the temperature changes from T_0 to T. Naturally, as the temperature increases, volumetric expansion occurs, and as the temperature decreases, contraction occurs. This situation can be expressed as in Eq. (6):

$$V_T = V_0 e^{\partial(T-T_0)} \tag{7}$$

In addition, during cryogenic cooling, crystal lattice contraction induces internal stresses and plastic deformation, primarily due to the presence of heterogeneous phases and differences in thermal expansion coefficients between grains. This process contributes to the reduction of micropore defects. Moreover, when the accumulated dislocations at the original grain boundaries -resulting from increased internal stress and plastic deformation - exceed the threshold stress required for recrystallization, grain splitting occurs, leading to grain refinement [64]. As a result, the total grain boundary length increases, which hinders dislocation movement and thereby enhances the material's strength. Another notable effect of cryogenic cooling is its ability to relieve stress concentrations at grain boundaries by promoting a more uniform distribution of dislocations. This reduces the resistance to dislocation motion during deformation, ultimately improving the material's ductility [61]. The highest H/E and H^3/E^2 values in Table 3 clearly demonstrate the increase in ductility at cryogenic temperatures, as stated in the literature and theoretically explained. This case is achieved thanks to increased hardness and elastic modulus. Thus, it can be said that, despite reaching the highest contact pressures at cryogenic temperature, the increase in plastic deformation and crack resistance results in less wear debris and a smoother surface, leading to a lower wear rate.

3.3. Worn surface analysis

3.3.1. Effects of as-built texture and applied load on the wear behavior of LPBF samples tested at room temperature

In order to evaluate the wear behavior of samples with different textures resulting from the applied different laser energy densities, wear tests were performed on the samples as produced without any grinding or polishing process. SEM images of the worn surface obtained from the wear tests performed at room temperature and under two different loads (5 N, 10 N) are given in Fig. 10 and Fig. 11, respectively. Examination of Fig. 10 reveals distinct wear features on the worn surfaces of the LPBF samples subjected to a 5 N load. In the LPBF-1 sample (Fig. 10b), wear debris, delamination, and spallation-related damage are evident. The LPBF-2 sample (Fig. 10d) exhibits more pronounced wear, characterized by extensive spallation, exfoliation, and visible porosity. The LPBF-3 surface displays the most severe wear, with the coarsest abrasive marks observed among the three. These observations align with the data presented in Table 3, indicating increased brittleness or low fracture toughness (as reflected by the H/E ratio), and reduced resistance to plastic deformation (lower H^3/E^2 ratio). As the load increases to 10 N, it is observed that more abrasive wear occurs, especially in the middle region of the contact mark where the maximum compressive stress occurs, on all three sample surfaces produced with different laser energy densities (Fig. 11b, d, f). However, increased spallation, delamination and abrasive wear marks were observed in the LPBF-2 and LPBF-3 samples with lower fracture toughness and plastic deformation resistance. This behavior is likely attributed not only to the increased applied load but also to the combined effects of cyclic compressive and tangential frictional stresses generated during the reciprocating wear test.

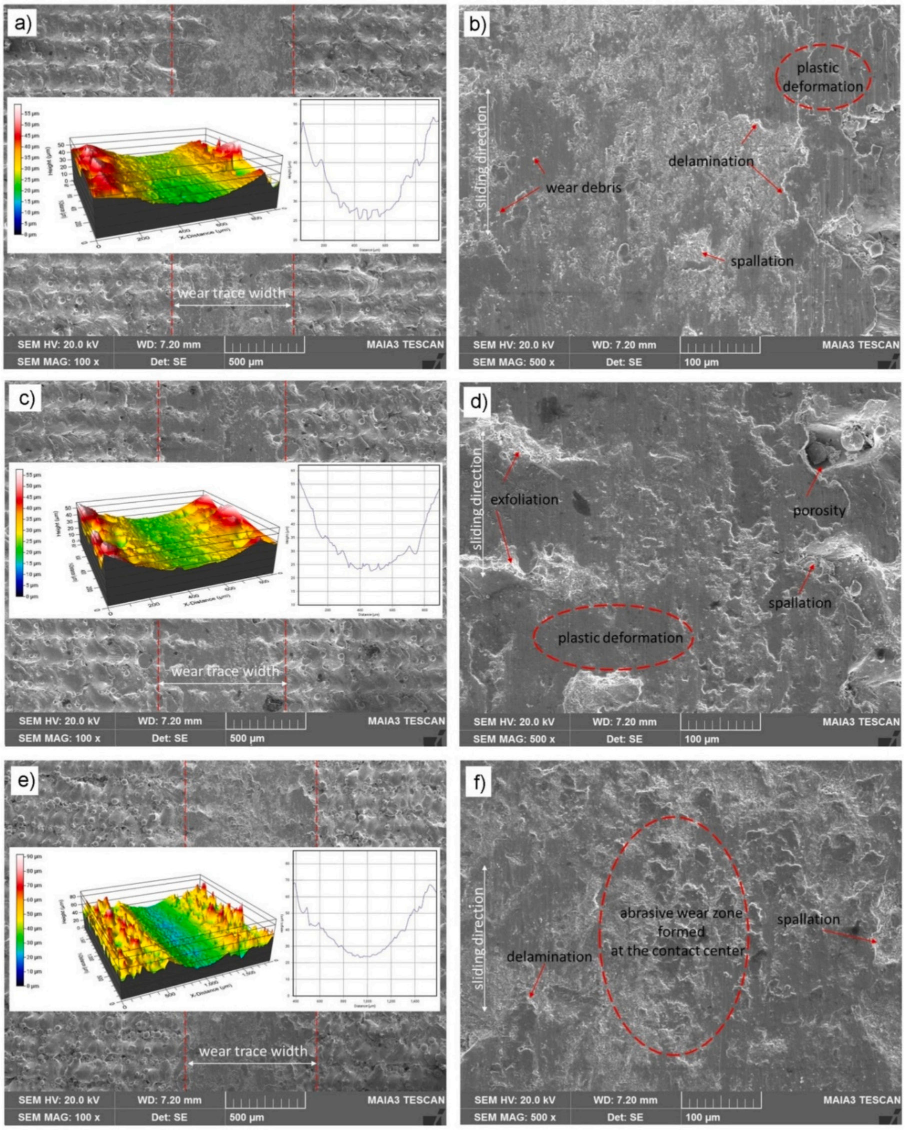

Fig. 10. Worn surface SEM images taken after the wear tests at room temperature (Load: 5 N). The images in (a,c,e) represent LPBF-1, LPBF-2, and LPBF-3 test samples. The micrographs in (b,d,f) are high-magnification images of those given in (a,c,e), respectively.

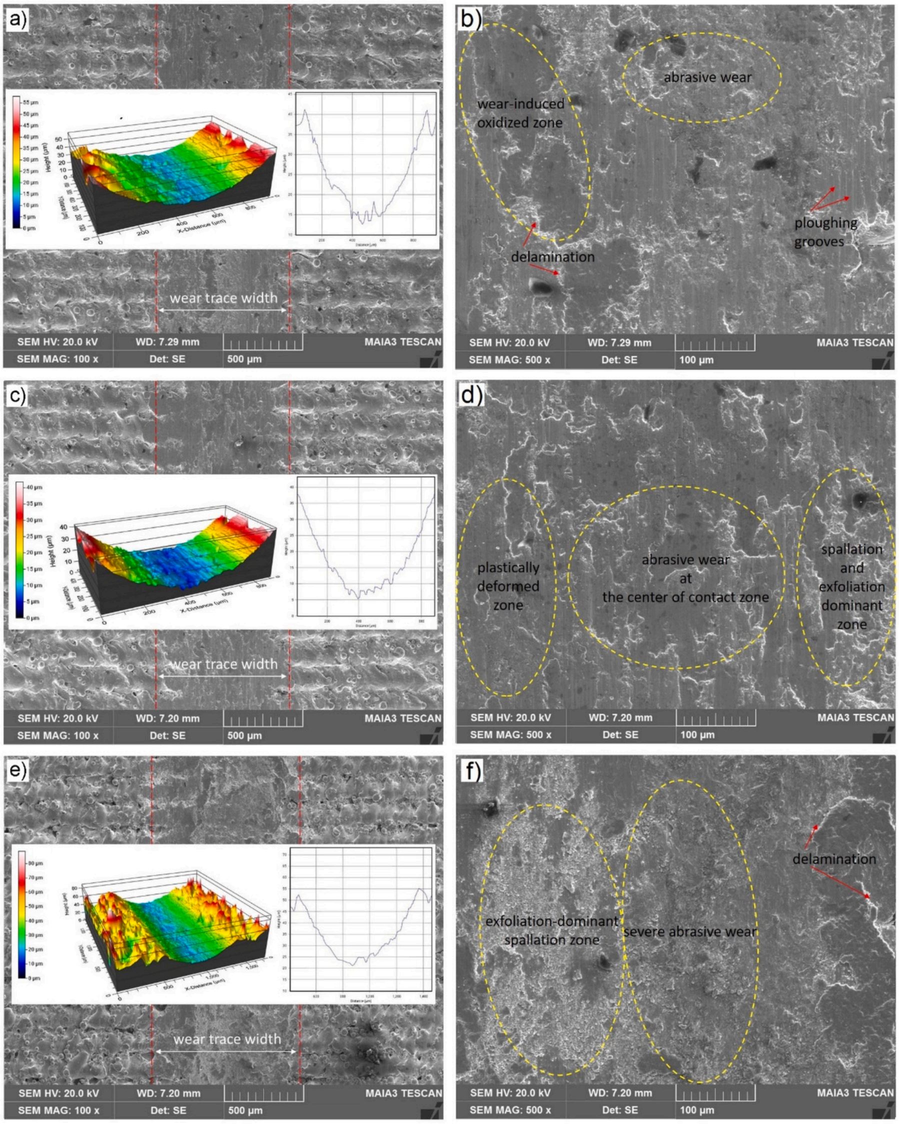

Fig. 11. Worn surface SEM images taken after the wear tests at room temperature (Load: 10 N). The images in (a,c,e) represent LPBF-1, LPBF-2, and LPBF-3 test samples. The micrographs in (b,d,f) are high-magnification images of those given in (a,c,e), respectively.

Particularly as depicted in the SEM micrograph of the worn surface of LPBF-3 given in Fig. 11f, exfoliation-dominant spallation and delamination formation are more evident in the scar edge region, while severe abrasive wear occurs in the scar center.

3.3.2. Effect of low (−40 °C) and cryogenic (−150 °C) ambient temperatures on wear behavior

Fig. 12 presents SEM micrographs of the worn surfaces obtained after wear tests performed at ambient temperatures of −40 °C and − 150 °C.

Examination of the wear images in Fig. 12 reveals a notable difference in the wear characteristics at −40 °C and − 150 °C. This trend is consistent across all LPBF-1, LPBF-2, and LPBF-3 samples. At −40 °C, significant wear debris accumulation is observed, indicating more severe surface degradation. In contrast, at −150 °C, the worn surfaces appear considerably smoother, suggesting a reduction in wear severity under cryogenic conditions. The temperature difference between the two ambient conditions appears to be the primary factor influencing the wear behavior. For the LPBF-1 sample, unlike the surface observed at room temperature under the same 10 N load (Fig. 13), friction-induced oxidation is notably suppressed at −40 °C. However, increased wear debris formation at this temperature, mainly due to the highest contact pressure, occurred across all ambient temperatures. In the case of the LPBF-1 sample, a shallower indentation depth was observed at −150 °C, likely due to increased hardness at this temperature. This is further supported by the presence of irregular regions between the laser scan pass boundaries. Another notable observation, as previously mentioned, is that shrinkage and increased internal stresses at cryogenic temperatures influence dislocation accumulation at grain boundaries, ultimately enhancing ductility [58,61]. Evidence of this increased ductility is the clear presence of a smearing-type wear mechanism. Additionally, longitudinal tearing marks along the smear lines indicate facilitated plastic deformation in the sliding direction, further supporting the occurrence of enhanced ductility under these conditions. For the LPBF-2 sample, a dense accumulation of wear debris is observed across the entire wear track width at an ambient temperature of −40 °C. Notably, along the midline of the track - where contact pressure is highest - abrasion flakes resulting from ploughing and smearing are evident. At the cryogenic temperature of −150 °C, the most prominent feature on the worn surface is the presence of exfoliation and spallation wear mechanisms, particularly along the adjacent laser scan boundaries oriented perpendicular to the sliding direction. This behavior can be attributed to unmelted particles and incomplete fusion along the laser scan boundaries,

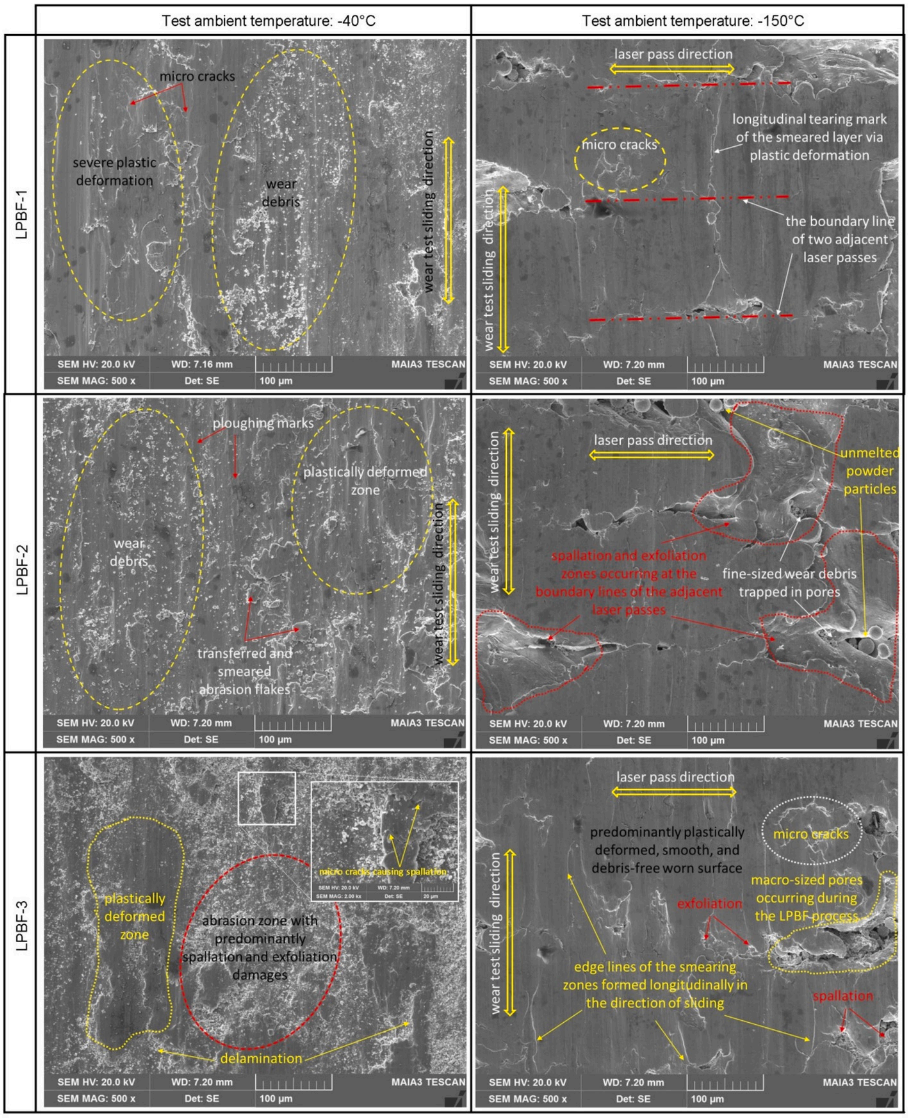

Fig. 12. Worn surface SEM images taken after the wear tests at −40 °C and − 150 °C ambient temperatures (Load: 10 N). According to these results, it looks like the wear damage is still on the surface, does not diffuse to the underlying microstructure.

resulting from the relatively low laser energy density. Examination of the worn surfaces of the LPBF-3 sample reveals dense wear debris formation - similar to that observed in the LPBF-2 sample at −40 °C - as well as wear features consistent with spallation and exfoliation mechanisms. This behavior can be attributed to the previously discussed low fracture toughness of the LPBF-3 sample, as indicated by its H/E ratio, as well as the presence of a plastic deformation zone on the surface resulting from its relatively low resistance to plastic deformation, reflected by the H^3/E^2 ratio. It is also evident that crack formation under high contact pressure and the corresponding shear stress, leading to greater spallation and exfoliation, plays a significant role in the wear behavior. At cryogenic temperature, the LPBF-3 sample exhibits the highest wear rate compared to the LPBF-2 and LPBF-3 samples. This case is primarily attributed to the combined effect of its relatively finer grain size and the highest contact pressure due to the reduction of Poisson's ratio from 0.3 to 0.25 with decreasing ambient temperature. Another striking feature is the macropore formation observed on the LPBF-3 worn surface, likely resulting from the lowest laser energy density used in this study. Additionally, numerous longitudinal lines consistent with smearing edges appear along the sliding direction, further indicating that plastic deformation is the dominant wear mechanism. In summary, at an ambient temperature of −40 °C, compared to room temperature, the partial increase in contact pressure results in higher shear stress, leading to greater spallation, delamination, and exfoliation wear mechanisms and yielding a higher wear rate. These processes involve brittle fracture, and it was observed that wear debris spreads across the entire contact area. Conversely, at −150 °C, the volume loss is minimized due to the combined effects of increased hardness and ductility. This is in good agreement with the smooth, debris-free worn surfaces observed at cryogenic temperatures, where smeared and transferred flakes are clearly visible.

Examination of the EDS analyses in Fig. 13 reveals clear friction-induced oxidation on the wear track surface at room temperature, whereas no oxide formation is observed at ambient temperatures of −40 °C and − 150 °C. This confirms the presence of oxidative wear at room temperature. In this wear mode, the oxide layer acts as a solid lubricant, reducing friction. However, wear traces from broken hard oxide particles are also evident, caused by both ploughing and rolling types of three-body abrasion.

4. Conclusions

In this study, Inconel 718 samples were fabricated using the Laser Powder Bed Fusion (LPBF) technique—an additive manufacturing

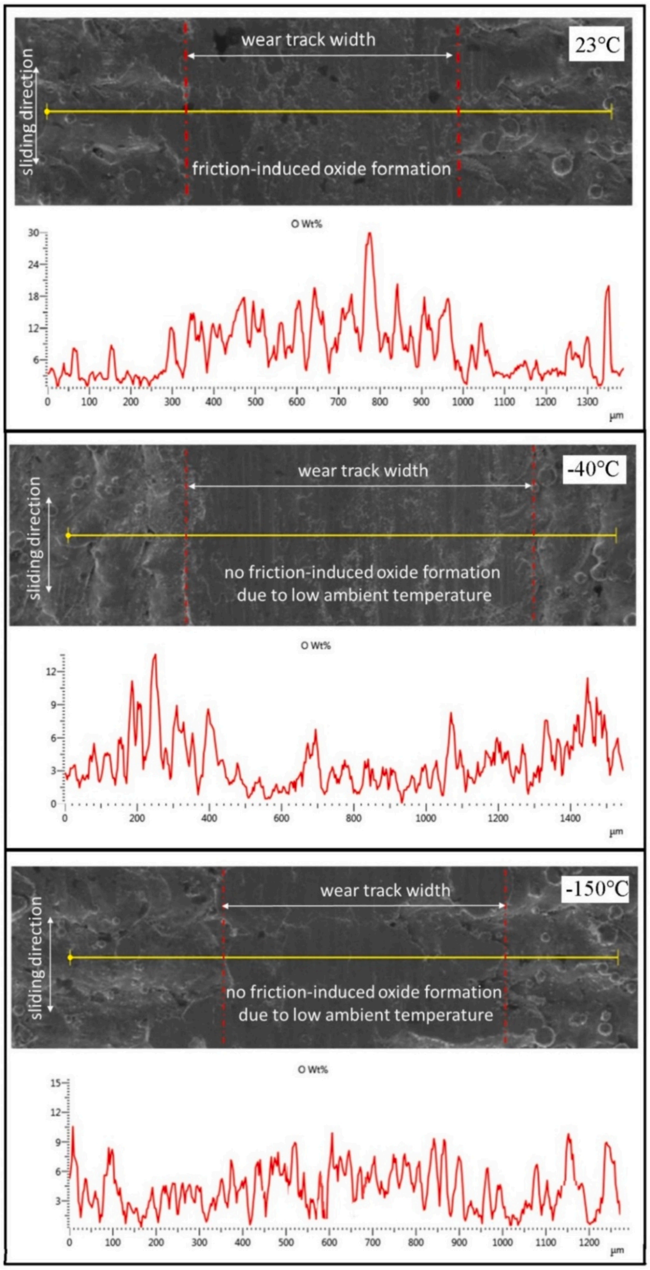

Fig. 13. EDS line analyzes of the worn surface SEM images taken after the wear tests at different ambient temperatures (Load: 10 N).

method—under varying laser energy densities achieved through different combinations of laser power and scanning speed. The resulting samples were designated as LPBF-1, LPBF-2, and LPBF-3, in descending order of applied laser energy density. The effects of surface texture and mechanical properties of the produced samples on wear behavior at room, low and cryogenic ambient temperatures were investigated. The findings can be summarized as follows:

- The variation in microstructural features was related to the laser energy input, shaping the melt pool, and thus resulting in different crystallographic orientation. Moreover, the unique microstructural features to LPBF process exhibited major <101> and minor <001> lamella microstructure with smaller grain size for strengthening and low Young's modulus owing to the texture characteristics.
- It was determined that the nanohardness (H) values increased with rising laser energy density. The highest hardness was observed in the LPBF-1 sample, which was produced with the highest laser energy density, followed by the LPBF-2 and LPBF-3 samples in descending order, consistent with the applied energy densities.
- The elastic modulus (E) values of the LPBF samples were found to be inversely proportional to the applied laser energy density.
- LPBF-1 sample gave the lowest specific wear rate at all ambient temperatures studied. LPBF-2 and LPBF-3 samples produced using the medium and lowest laser energy density had higher wear rates at all temperatures, in the same order. These results are also quite consistent with the H/E and H^3/E^2 ratios of the respective samples.
- Regarding the effect of ambient temperature on wear rate and wear mechanisms, the wear volume loss at −40 °C ambient temperature was the highest in all LPBF samples compared to those at RT and cryogenic temperatures. While severe plastic deformation, delamination and abrasive wear were dominant at RT, the presence of wear debris spread over the entire surface was noticeable at −40 °C ambient temperature. It was also observed that intense spallation and exfoliation type wear was effective. At cryogenic ambient temperature, a smoother wear surface was obtained with the effect of increased ductility, valid for all three samples. The general appearance of plastering and transfer film on the worn surface is remarkable, and spallation and exfoliation type wear is observed to be evident in the incomplete fusion regions at the laser scan borders in proportion to the decreasing laser energy density.
- While COF values very close to each other were obtained at RT and − 40 °C ambient temperatures, COF values at cryogenic ambient temperature were quite low.
- Oxide formation due to friction was observed on the worn surface at room temperature (RT), while no oxide formation occurred at low and cryogenic ambient temperatures.

CRediT authorship contribution statement

Yılmaz Küçük: Writing – original draft, Methodology, Formal analysis. **Ozkan Gokcekaya:** Writing – original draft, Investigation, Data curation, Visualization, Conceptualization. **Ali Günen:** Writing – original draft, Visualization, Validation, Investigation, Conceptualization. **Mustafa Sabri Gök:** Validation, Supervision, Formal analysis. **Abdollah Bahador:** Supervision, Methodology, Investigation. **Takayoshi Nakano:** Methodology, Investigation, Resources. **Gürel Çam:** Validation, Supervision, Conceptualization.

Declaration of competing interest

The authors declare that they have no known competing financial interests or personal relationships that could have appeared to influence the work reported in this paper.

Acknowledgements

This work was supported by CREST-Nanomechanics: Elucidation of macroscale mechanical properties based on understanding nanoscale dynamics of innovative mechanical materials (Grant Number: JPMJCR2194) from the Japan Science and Technology Agency (JST).

References

[1] Dhanola A, Khanna N, Gajrani KK. A critical review on liquid superlubricitive technology for attaining ultra-low friction. Renew Sust Energ Rev 2022;165: 112626.
[2] Animah I, Shafiee M. Application of risk analysis in the liquefied natural gas (LNG) sector: an overview. J Loss Prev Process Ind 2020;63:103980.
[3] Dhokey NB, Upadhye A, Shah N, Tharian KT. Transition in wear behavior and mechanical properties of novel high nitrogen martensitic steel in cryogenic temperature regimes. Mater Today Proc 2021;43:3023–9.
[4] Gokcekaya O, Günen A, Ceritbinmez F, Bahador A, Nakano T, Çetin M. Wire-EDM performance and surface integrity of Inconel 718 with unique microstructural

features fabricated by laser powder bed fusion. Int J Adv Manuf Technol 2024;130 (9):4513–28.
[5] Lindner T, Günen A, Töberling G, Vogt S, Karakas MS, Löbel M, et al. Boriding of laser-clad Inconel 718 coatings for enhanced wear resistance. Appl Sci 2021;11 (24):11935.
[6] Hosseini E, Popovich VA. A review of mechanical properties of additively manufactured Inconel 718. Addit Manuf 2019;30:100877.
[7] Günen A, Gürol U, Çakan A, Koçak M, Çam G, Yildizhan H, et al. Effect of post-deposition aluminizing on the corrosion and mechanical behavior of WAAM-fabricated stainless steel and Ni-based superalloy. Sci Rep 2025;15:43268.
[8] Karakas MS, Günen A, Lindner T, Küçük Y, Kon Ö, Joshi S, et al. Comparative study of heat treatment routes for enhancing high-temperature wear resistance of EBM-processed Inconel 718. Mater Today Commun 2025;49:113864.
[9] Qi X, Li Y, Li F, Du J, Niu J, Fan W, et al. Regulating strength and ductility of additively manufactured Inconel 718 alloy via adding nano-TiC and deep cryogenic treatment. Mater Sci Eng A 2024;910:146852.
[10] Gokcekaya O, Ishimoto T, Hibino S, Yasutomi J, Narushima T, Nakano T. Unique crystallographic texture formation in Inconel 718 by laser powder bed fusion and its effect on mechanical anisotropy. Acta Mater 2021;212:116876.
[11] Nazir A, Gokcekaya O, Billah KMM, Ertugrul O, Jiang J, Sun J, et al. Multi-material additive manufacturing: a systematic review of design, properties, applications, challenges, and 3D printing of materials and cellular metamaterials. Mater Des 2023;226:111661.
[12] Cam G, Gunen A. Challenges and opportunities in the production of magnesium parts by directed energy deposition processes. J Magnesium Alloys 2024;12: 1663–86.
[13] Cam G. Prospects of producing aluminum parts by wire arc additive manufacturing (WAAM). Mater Today Proc 2022;62(1):77–85.
[14] Ishimoto T, Morita N, Ozasa R, Matsugaki A, Gokcekaya O, Higashino S, et al. Superimpositional design of crystallographic textures and macroscopic shapes via metal additive manufacturing—game-change in component design. Acta Mater 2025;286:120709.
[15] Liu B, Xu J, Gao Y, Hu Y, Yang X, Ding Y, et al. Fine grains with high-density annealing twins and precipitates inducing favorable strength and excellent plasticity in laser powder bed fusion-fabricated Inconel 718 via deep cryogenic and heat treatments. J Mater Sci Technol 2024;187:28–48.
[16] Eren Z, Gokcekaya O, Balkan D, Nakano T, Mecitoğlu Z. Comparison of in-plane compression of additively manufactured Ti6Al4V 2D auxetic structures: lattice design, manufacturing speed, and failure mode. Mater Des 2024;241:112885.
[17] Samuel C, Arivarasu M, Prabhu TR. High temperature dry sliding wear behaviour of laser powder bed fused Inconel 718. Addit Manuf 2020;34.
[18] Naskar S, Suryakumar S, Panigrahi BB. Heat treatments-induced wear resistance of Inconel 718 superalloy fabricated via laser based powder bed fusion. Mater Today Commun 2024;41:110789.
[19] Blakey-Milner B, Gradl P, Snedden G, Brooks M, Pitot J, Lopez E, et al. Metal additive manufacturing in aerospace: a review. Mater Des 2021;209:110008.
[20] Bulutsuz AG, Gulec B, Gokcekaya O, Gardstam J, Nakano T, Yilmazer H. An investigation over microstructure and HIP processing effects on wear performance of pure chromium parts fabricated by laser powder bed fusion. Int J Refract Met Hard Mater 2024;120:106616.
[21] Kocaman E, Gurol U, Gunen A, Cam G. Effect of post-deposition heat treatments on high-temperature wear and corrosion behavior of Inconel 625. Mater Today Commun 2025;42:111101.
[22] Oliver WC, Lucas BN, Pharr GM. Mechanical characterization using indentation experiments. In: Mechanical properties and deformation behavior of materials having ultra-fine microstructures. Dordrecht: Springer Netherlands; 1993. p. 417–28.
[23] Sharma S, Palaniappan K, Mishra VD, Vedantam S, Murthy H, Rao BC. Effect of process parameters on texture in quasi-isotropic IN718 processed by laser powder bed fusion. J Manuf Sci Eng 2025;147(7):071003.
[24] Dwivedi A, Khurana MK, Bala YG, Mishra SB. Influence of modified heat treatment on microstructure, hardness and wear resistance of Inconel 718 fabricated by powder bed fusion-laser beam additive manufacturing process. J Mater Eng Perform 2025:1–17. https://doi.org/10.1007/s11665-025-11290-7.
[25] Pérez-Ruiz JD, Galbusera F, Caprio L, Previtali B, de Lacalle LNL, Lamikiz A, et al. Laser beam shaping facilitates tailoring the mechanical properties of IN718 during powder bed fusion. J Mater Process Technol 2024;328:118393.
[26] Al-Lami J, Dessolier T, Rogers SR, Pirzada T, Pham MS. Dislocation distribution, crystallographic texture evolution, and plastic inhomogeneity of Inconel 718 fabricated by laser powder bed fusion. Adv Eng Mater 2024;27(9):2400524.
[27] Lane B, Heigel J, Ricker R, Zhirnov I, Khromschenko V, Weaver J, et al. Measurements of melt pool geometry and cooling rates of individual laser traces on IN625 bare plates. Integr Mater Manuf Innov 2020;9:16–30.
[28] Khorasani M, Ghasemi A, Leary M, Cordova L, Sharabian E, Farabi E, et al. A comprehensive study on meltpool depth in laser-based powder bed fusion of Inconel 718. Int J Adv Manuf Technol 2022;120(3):2345–62.
[29] Wang J, Zhu R, Liu Y, Zhang L. Understanding melt pool characteristics in laser powder bed fusion: an overview of single-and multi-track melt pools for process optimization. Adv Powder Mater 2023;2(4):100137.
[30] Joshy J, Kuriachen B. Effect of heat treatment and cryo-treatment on dry tribological behavior of Inconel 718 fabricated using laser powder bed fusion. Wear 2023;523:204819.
[31] Tayon WA, Shenoy RN, Redding MR, Keith Bird R, Hafley RA. Correlation between microstructure and mechanical properties in an Inconel 718 deposit produced via electron beam freeform fabrication. J Manuf Sci Eng 2014;136(6):061005.
[32] Parimi LL, Ravi GA, Clark D, Attallah MM. Microstructural and texture development in direct laser fabricated IN718. Mater Charact 2014;89:102–11.
[33] Schirra JJ. Effect of heat treatment variations on the hardness and mechanical properties of wrought Inconel 718. Superalloys 1997;718(706):431–8.
[34] Radhakrishnan B, Thompson RG. Solidification of the nickel-base superalloy 718: a phase diagram approach. Metall Trans A 1989;20:2866–8.
[35] Chlebus E, Gruber K, Kuźnicka B, Kurzac J, Kurzynowski T. Effect of heat treatment on the microstructure and mechanical properties of Inconel 718 processed by selective laser melting. Mater Sci Eng A 2015;639:647–55.
[36] Popovich VA, Borisov EV, Popovich AA, Sufiiarov VS, Masaylo DV, Alzina L. Impact of heat treatment on mechanical behaviour of Inconel 718 processed with tailored microstructure by selective laser melting. Mater Des 2017;131:12–22.
[37] Zhou L, Mehta A, McWilliams B, Cho K, Sohn Y. Microstructure, precipitates and mechanical properties of powder bed fused inconel 718 before and after heat treatment. J Mater Sci Technol 2019;35(6):1153–64.
[38] Mayama T, Ishimoto T, Tane M, Cho K, Manabe K, Miyashita D, et al. Novel strengthening mechanism of laser powder bed fusion-manufactured Inconel 718: effects of customized hierarchical interfaces. Addit Manuf 2024;93:104412.
[39] Weng Z, Gu K, Cui C, Cai H, Liu X, Wang J. Microstructure evolution and wear behavior of titanium alloy under cryogenic dry sliding wear condition. Mater Charact 2020;165:110385.
[40] Vieille B, Keller C, Mokhtari M, Briatta H, Breteau T, Nguejio J, et al. Investigations on the fracture behavior of Inconel 718 superalloys obtained from cast and additive manufacturing processes. Mater Sci Eng A 2020;790:139666.
[41] DebRoy T, Wei HL, Zuback JS, Mukherjee T, Elmer JW, Milewski JO, et al. Additive manufacturing of metallic components–process, structure and properties. Prog Mater Sci 2018;92:112–224.
[42] Lewandowski JJ, Seifi M. Metal additive manufacturing: a review of mechanical properties. Annu Rev Mater Res 2016;46(1):151–86.
[43] Boughrara N, Benzarti Z, Khalfallah A, Evaristo M, Cavaleiro A. Comparative study on the nanomechanical behavior and physical properties influenced by the epitaxial growth mechanisms of GaN thin films. Appl Surf Sci 2022;579:152188.
[44] Benzarti Z, Khalfallah A, Bougrioua Z, Evaristo M, Cavaleiro A. Understanding the influence of physical properties on the mechanical characteristics of Mg-doped GaN thin films. Mater Chem Phys 2023;307:128182.
[45] Leyland A, Matthews A. On the significance of the H/E ratio in wear control: a nanocomposite coating approach to optimised tribological behaviour. Wear 2000; 246(1–2):1–11.
[46] Beake BD. The influence of the H/E ratio on wear resistance of coating systems–insights from small-scale testing. Surf Coat Technol 2022;442:128272.
[47] Zhang S, Yan M, Yang Y, Zhang Y, Yan F, Li H. Excellent mechanical, tribological and anti-corrosive performance of novel Ti-DLC nanocomposite thin films prepared via magnetron sputtering method. Carbon 2019;151:136–47.
[48] Wang Y, Wang X, Shang H, Liu X, Qi Y, Qi X, et al. Impact of Ni doping on the microstructure and mechanical properties of TiB2 films. Nanomaterials (Basel, Switzerland) 2025;15(3):229.
[49] Malin CO, Schmidt EH. In: National Aeronautics and Space [Administration], editor. Tensile and fatigue properties of Inconel 718 at cryogenic temperatures (NASA tech brief 69-10068); 1969.
[50] https://salomons-metalen.com/products/inconel-718 (access date: March 6, 2026) Salomons Metalen B.V. Alloy 718: UNS N07718/W.Nr. 2.4668 data sheet.
[51] Park SY, Kim KS, Kim MC, Kassner ME, Lee KA. Effect of post-heat treatment on the tensile and cryogenic impact toughness properties of inconel 718 manufactured by selective laser melting. Adv Eng Mater 2021;23(3):2001005.
[52] Balachandramurthi AR, Moverare J, Mahade S, Pederson R. Additive manufacturing of alloy 718 via electron beam melting: effect of post-treatment on the microstructure and the mechanical properties. Materials (Basel, Switzerland) 2018;12(1):68.
[53] Dubey D, Mukherjee R, Singh MK. A review on tribological behavior of nickel-based Inconel superalloy. Proc Instit Mech Eng J J Eng Tribol 2024;238(6):706–32.
[54] Jiang X, Lu J, Zhao N, Chen Z, Zhao Z. A review of wear in additive manufacturing: wear mechanism, materials, and process. Lubricants 2024;12(9):321.
[55] Küçük Y. Effect of counter body on wear behavior of plasma-sprayed TiO2-45Cr2O3 coating. J Asian Ceramic Soc 2021;9(1):237–52.
[56] Küçük Y. Effect of counterbody on the dry sliding wear performance of plasma sprayed calcia-stabilized zirconia coating. Int J Refract Met Hard Mater 2020;92: 105284.
[57] Hertz H. On the contact of elastic solids. J Reine Angew Math 1881;92:156–71 [Translated and reprinted in English in Hertz's Miscellaneous Papers, Macmillan & Co., London, 1896 Ch. 5].
[58] Johnson KL. Contact mechanics. Cambridge, U.K.: Cambridge University Press; 1985.
[59] Kucuk Y. Investigation of abrasiveness property of blast furnace slag on ceramic coatings via the abrasive slurry wear method. Tribol Trans 2012;55(6):762–71.
[60] Balachandramurthi AR, Moverare J, Dixit N, Pederson R. Influence of defects and as-built surface roughness on fatigue properties of additively manufactured alloy 718. Mater Sci Eng A 2018;735:463–74.
[61] Qi X, Li Y, Li F, Du J, Niu J, Fan W, et al. Regulating strength and ductility of additively manufactured Inconel 718 alloy via adding nano-TiC and deep cryogenic treatment. Mater Sci Eng A 2024;910:146852.

[62] Zakarian D, Khachatrian A. Temperature dependence of the hardness of materials with a metallic, covalent-metallic bonds. Metal Powder Report 2021;76(6):26–31.

[63] Han B, Zhang C, Feng K, Li Z, Zhang X, Shen Y, et al. Additively manufactured high strength and ductility CrCoNi medium entropy alloy with hierarchical microstructure. Mater Sci Eng A 2021;820:141545.

[64] Li H, Zhao W, Chen T, Huang Y, Sun J, Zhu P, et al. Beneficial effects of deep cryogenic treatment on mechanical properties of additively manufactured high entropy alloy: cyclic vs single cryogenic cooling. J Mater Sci Technol 2022;115: 40–51.